energy&fuels

Article

Cite This: Energy Fuels 2017, 31, 11448-11459

pubs.acs.org/EF

Impact of Gaseous Chemistry in $H_2-O_2-N_2$ Combustion over Platinum at Fuel-Lean Stoichiometries and Pressures of 1.0−3.5 bar

Ran Sui, John Mantzaras,* Et-touhami Es-sebbar, Mohammad A. Safi, and Rolf Bombach

Laboratory of Thermal Processes and Combustion, Paul Scherrer Institute, CH-5232 Villigen PSI, Switzerland

ABSTRACT: The catalytic and gas-phase combustion of fuel-lean $H_2-O_2-N_2$ premixtures was investigated in a channel coated with platinum at pressures 1.0−3.5 bar, a range encompassing microreactors in portable power generation systems and passive hydrogen recombiners in nuclear power plants. One-dimensional Raman spectroscopy assessed the progress of catalytic hydrogen combustion, while planar laser-induced fluorescence (LIF) of the hydroxyl radical monitored gaseous combustion. Simulations were performed using a 2-D code with detailed catalytic and gas-phase reaction mechanisms and realistic transport. Both LIF measurements and simulations revealed that homogeneous combustion was vigorously sustained below ∼2.5 bar, while it was effectively suppressed at higher pressures. This was due to the intricate pressure dependency of the hydrogen gaseous ignition chemistry and the competition between catalytic and gaseous chemical reactions for hydrogen consumption. Parametric simulations determined the smallest critical channel heights allowing for appreciable gaseous combustion and their dependency on pressure, wall temperature, and inlet velocity. It was shown that for the narrower channels of catalytic microreactors homogeneous combustion was relevant only for wall temperatures above 1300 K, whereas for the wider hydrogen recombiner channels it could be relevant for wall temperatures down to 1100 K. Furthermore, at 1100 K the critical channel heights were nonmonotonic functions of pressure, reaching their peaks at 2.0−2.5 bar.

1. INTRODUCTION

Hydrogen is currently investigated as a fuel for large power plants[1−3] and for microreactors in small-scale power generation.[4−7] Hydrogen in small power systems can be prepared on-board from hydrocarbons using microreformers.[8,9] While catalytic combustion is a choice for large power plants,[3,10,11] it is the mainstream approach for small power systems. This is primarily due to the increased surface-to-volume ratios of microreactors that promote surface catalytic reactions over volumetric gas-phase reactions. Moreover, several unwanted instabilities appearing during gaseous combustion in wall-bounded flows[12−14] can be suppressed when the microreactor surfaces are coated with a catalyst.[15,16]

Catalytic combustion of hydrogen is also of main concern for passive recombiners used in nuclear power plants.[17] In the event of a severe accident, the core meltdown releases hydrogen, steam, and other gases that can further pressurize the reactor containment up to about 3.5 bar. Catalytic recombiners (having noble metals as active catalysts) can efficiently convert the released hydrogen to steam, thus mitigating destructive explosions inside the reactor containment. A common feature of hydrogen catalytic reactors used for small power generation and for nuclear reactor safety is their modest operating pressures 1.0 to ∼3.5 bar. Catalytic combustion of hydrogen is especially demanding[18] because of the diffusional imbalance of hydrogen (H_2 has a Lewis number Le_{H2} ∼ 0.3 at lean mixtures in air), which results in superadiabatic surface temperatures[19,20] that compromise the reactor and the catalyst thermal stability.

The onset of homogeneous (gaseous) ignition inside catalytic reactors is of central interest. It has been established that homogeneous combustion moderates the catalytically induced superadiabaticity[20,21] which, depending on the specific application, can either be beneficial or detrimental. For nearly adiabatic system operation, homogeneous combustion can be advantageous in terms of microreactor thermal management by reducing the superadiabatic surface temperatures which are created by the heterogeneous reaction pathway. However, in strongly nonadiabatic systems, the moderating effect of homogeneous combustion is unfavorable since it lowers the temperatures at the catalyst surface and hence reduces the associated heat transfer (e.g., when using the heat radiated from the microreactor surfaces to power thermophotovoltaics[5]). In such cases the onset of gaseous combustion compromises the microreactor performance. On the other hand, homogeneous ignition in catalytic hydrogen recombiners of nuclear power plants is always detrimental[22] as it may cause uncontrolled explosion in the reactor containment.

The kinetics of hydrogen over platinum (which is the herein used catalyst) has been intensely investigated, leading to the construction of mean-field detailed heterogeneous chemical mechanisms.[23−25] The progress in hydrogen catalytic kinetics has further been assisted by ab initio simulations[26,27] and in situ surface science measurements.[28] Moreover, recent studies have improved the homogeneous hydrogen mechanisms especially at elevated pressures pertinent to power generation.[29−31] Nonetheless, there are fewer fundamental works for coupled catalytic and gas-phase hydrogen combustion.

For lean H_2/air stoichiometries, Bui et al.[19] numerically studied homogeneous ignition over Pt-coated surfaces in stagnation point flow configurations at ambient pressure and determined the key hetero/homogeneous chemical interactions. Appel et al.[20] measured, by means of laser diagnostics,

Received: July 12, 2017
Revised: September 19, 2017
Published: September 19, 2017

DOI: 10.1021/acs.energyfuels.7b02011
Energy Fuels 2017, 31, 11448−11459

minor and major gas-phase species concentrations in a Pt-coated channel at ambient pressure and with the aid of numerical simulations assessed several heterogeneous and gas-phase mechanisms and especially their suitability in capturing homogeneous ignition. The foregoing atmospheric-pressure works were subsequently extended[32,21] to 15 bar, focusing mainly on large-scale power generation and on gas-turbine-pertinent conditions. Detailed hydrogen hetero/homogeneous combustion studies are still needed in the lower pressure range 1.0−3.5 bar, which is relevant to catalytic microreactors and recombiners. This is especially important as the complex hydrogen gas-phase ignition chemistry exhibits its strongest pressure dependence in the range from 1.0 to ∼3.5 bar for temperatures of up to 1100 K that are relevant to catalytic systems.[21]

The present work investigates experimentally and numerically the heterogeneous and homogeneous combustion of lean $H_2/O_2/N_2$ mixtures on Pt at pressures 1.0−3.5 bar, with measurements in fine increments of 0.5 bar. A rectangular catalytic reactor with a height of 7 mm was used in the experiments. Raman spectroscopy was applied to determine the 1-D profiles (across the 7 mm height of the catalytic channel) of major gaseous species concentrations, and planar laser-induced fluorescence assessed the OH radical concentration in the streamwise plane of symmetry. Simulations were performed using a 2-D numerical code with detailed heterogeneous and homogeneous chemical mechanisms and realistic transport. Main goals were to evaluate the effects of pressure on the gas-phase ignition propensity and to deliver validated heterogeneous and homogeneous chemical reaction mechanisms. An additional goal was to delineate the regimes of significant gas-phase combustion and their dependence on the confinement of the channel geometry (channel height) and on the operating variables (pressure, wall temperature, inlet velocity, and equivalence ratio).

Section 2 describes the experimental approach and Section 3 the simulation tools, while the results follow in Section 4. Measurements are compared against predictions in Section 4.1, and the pressure dependence of homogeneous ignition is elaborated in Section 4.2. The minimum critical channel heights necessary for significant gas-phase combustion are mapped as a function of operating parameters in Section 4.3, and the resulting implications for hydrogen catalytic microreactors and recombiners are discussed. The main conclusions are finally outlined in Section 5.

2. EXPERIMENTAL SETUP AND MEASURING TECHNIQUES

Experimental details have been provided elsewhere[33] such that a only basic description follows. The test rig (Figure 1) comprised a high-pressure channel reactor with optical accessibility and two laser setups, one for planar LIF of OH and the other for one-dimensional Raman spectroscopy of main gaseous species across the channel height.

Two horizontal ceramic Si[SiC] plates and two 3 mm thick quartz windows formed the catalytic reactor (Figure 1a). The length of the ceramic plates was 300 mm ($-x$), their width was 104 mm ($-z$), and their thickness was 9 mm. The distance between the two ceramic plates was 7 mm ($-y$). Plasma vapor deposition (PVD) was used to coat the inner surfaces of both ceramic plates, first by a 1.5 μm thick layer of nonporous alumina and then by a 2.2 μm thick layer of platinum. The alumina layer mitigated chemical interactions between Pt and Si. The considerably thick Pt coating behaved as polycrystalline platinum, and this was confirmed by active surface and total surface

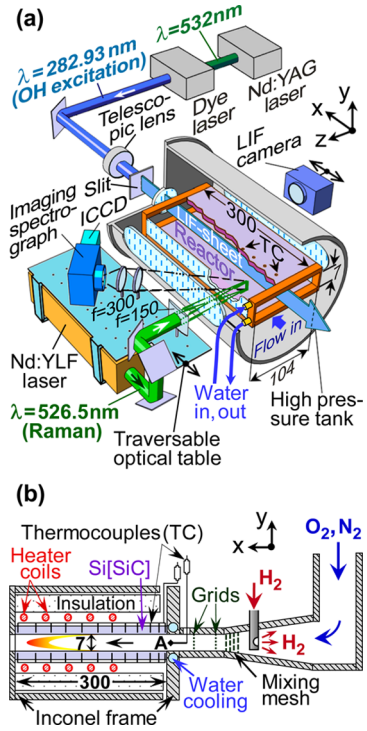

Figure 1. (a) Test rig with Raman/LIF laser setups and (b) reactor details (all dimensions in millimeters).

BET measurements (using CO chemisorption and Kr physisorption, respectively).[34]

The reactor was housed in a high-pressure cylindrical steel vessel equipped with two side windows made of quartz and having dimensions 350 × 50 × 35 mm^3. Two extra quartz windows, at the catalytic reactor exhaust and the rear vessel flange, yielded optical accessibility in the streamwise direction for the LIF excitation beam. To control the catalyst surface temperatures, a joint heating and cooling arrangement was employed. The outer ceramic surfaces were heated over the axial extent 100 mm < x < 300 mm by two resistive coils, each having adjustable power. On the other hand, the vertical entry sides of the ceramic plates were in contact to a water-cooled sector of an Inconel frame supporting the reactor (see Figure 1). Water cooling was essential to mitigate the surface temperature superadiabaticity that would have else been attained at the channel entry as a result of the hydrogen diffusional imbalance.[20] Twelve S-type thermocouples in each ceramic plate, positioned at the $x-y$ plane of symmetry (see Figure 1a) and fixed 0.9 mm underneath the catalyst, recorded the surface temperatures.

H_2, O_2, and N_2 flows have been regulated by means of three mass flow controllers. High-purity H_2 (99.995%) was introduced to an O_2/N_2 premixed flow inside a conical steel unit with a length of 200 mm, using eight 0.5 mm diameter horizontal nozzles positioned along the spanwise z-direction (see Figure 1b). The conical section, which was constructed to mitigate autoignition of the reactive gases, progressively adjusted its cross section from a circular shape (diameter of 35 mm) to the 104 × 7 mm^2 cross-flow rectangular channel area. The $H_2/O_2/N_2$ flow passed through a mesh with a thickness of 3 mm and then through two grids, ensuring mixture homogeneity and flow uniformity at the reactor entry. Optimization of the mesh and grid positions was accomplished with hot wire anemometry that verified the uniformity of the flow and planar LIF of the NO radical that attested a good mixing quality.[35,36] The NO was doped into the H_2 stream; the LIF excitation wavelength was 226.25 nm, and fluorescence detection was in the range 240−265 nm.

The experimental conditions (see Table 1) encompassed H_2:O_2 equivalence ratios φ = 0.20−0.28, pressures p = 1.0−3.5 bar, and N_2:O_2 vol. ratios 3.76−5.24. A K-type thermocouple (marked "A" in

DOI: 10.1021/acs.energyfuels.7b02011
Energy Fuels 2017, 31, 11448−11459

Table 1. Experimental Conditions[a]

case	p	φ	U_{IN}	T_{IN}	H_2	O_2
1	1.0	0.20	3.1	329	7.7	19.4
2	1.0	0.28	3.2	328	9.3	16.6
3	1.5	0.20	2.0	318	7.8	19.3
4	1.5	0.28	1.9	325	9.4	16.5
5	2.0	0.25	1.5	320	8.4	16.7
6	2.0	0.28	1.4	327	9.4	16.5
7	2.5	0.20	1.1	312	6.7	16.9
8	2.5	0.28	1.1	327	9.4	16.5
9	3.0	0.20	1.0	312	6.7	16.9
10	3.0	0.25	1.0	313	8.4	16.7
11	3.5	0.20	1.1	312	8.5	15.2
12	3.5	0.25	0.9	319	8.4	16.7

[a]Pressure (bar), equivalence ratio, inlet velocity (m/s), inlet temperature (K), and inlet composition (% vol.) of H_2 and O_2 with balance N_2.

Figure 1b) having a radiation-shielded bead measured the inlet gas temperatures (T_{IN}). The T_{IN} ranged from 312 to 329 K due to a slight preheat of the conical mixing section via heat conduction from the hot catalytic reactor. The inlet velocities were U_{IN} = 0.9−3.2 m/s, yielding laminar flows with incoming Reynolds numbers (calculated using the inlet gas properties and the channel height $2b$ = 7 mm) in the range 1030−1550.

The Raman and LIF optical setups are illustrated in Figure 1a. For LIF of OH, the 532 nm radiation of a Nd:YAG pulsed laser (Quantel-YG781C20 CL-D-LNE3, 10 ns pulse, and 20 Hz repetition rate) pumped a tunable dye laser (Quantel-TDL90). The output of the dye laser was frequency-doubled to generate radiation at 282.93 nm (0.5 mJ pulse energy), which excited the $Q_1(6)$ band of the OH electronic transition $A^2\Sigma$ (ν = 1) ← $X^2\Pi$ (ν' = 0). The excitation beam was converted into a vertical light sheet that propagated in a counterflow direction at the x−y plane of symmetry (see Figure 1a and further[21,33,36]). Fluorescence from the 1−1 and 0−0 transitions of OH (308 and 314 nm, respectively) was collected at 90° by an intensified CCD camera (LaVision Imager Compact HiRes-IRO) through the high-pressure vessel and reactor side windows. Channel areas 100 × 7 mm^2 were recorded on the CCD chip, occupying 1360 × 70 pixels. To record the full reactor extent, the camera was traversed in 50 mm increments along the axial direction. As the experimental conditions were laminar and steady, the signal-to-noise (SN) ratios was increased by averaging 400 single-shot LIF images at each recording location.

For the Raman technique, the radiation of a Nd:YLF pulsed laser (Quantronix Darwin-Duo, repetition frequency 2 kHz) at 526.5 nm was used (35 mJ pulse energy and 120 ns duration). The laser bean was focused, by means of an f = 150 mm cylindrical lens, into a vertical line with a thickness of 0.3 mm that spanned the whole 7 mm height of the channel. The beam was offset laterally by 15 mm (−z direction) so as to enhance the collection angle and to reduce the beam steering induced by thermal gradients.[21,33] Collection of the scattered light was achieved at 50° by a spectrograph (Chromex-250i) and an accompanying intensified CCD camera (Princeton Instruments PI-MAX1024GIII). The laser, optics, and the spectrograph were positioned on an optical table that could be traversed along the axial direction (see Figure 1a), allowing for measurements over the extent 9 ≤ x ≤ 126 mm. The SN ratio was increased by integrating on the detector chip the light scatted from 400 000 laser pulses. The accuracy of the measurements was ±3% for concentrations greater than 3% vol. and ±8% for concentrations down to 0.5% vol. Raman measurements closer than 0.7 mm to the catalytic surfaces were rejected as they had too low SN ratios.

3. NUMERICAL MODELING

A Navier−Stokes (NS) two-dimensional steady CFD code has been employed.[7,21] Using 420 × 48 grids in a staggered mesh (for the 300 × 7 mm^2 domain at the x−y plane of symmetry), a grid-independent solution was reached. The 12 thermocouple measurements on each Si[SiC] plate were used to fit curves and construct the upper and lower wall temperature profiles, which were subsequently used as boundary conditions. The inlet species mass fractions, streamwise velocity, and temperature had all uniform profiles, whereas no-slip velocity conditions were applied at the gas−surface interfaces.

The governing equations are summarized below:

Continuity:

$$\frac{\partial(\rho u)}{\partial x} + \frac{\partial(\rho v)}{\partial y} = 0 \tag{1}$$

Momentum:

$$\frac{\partial(\rho uu)}{\partial x} + \frac{\partial(\rho vu)}{\partial y} + \frac{\partial p}{\partial x} - \frac{\partial}{\partial x}\left[2\mu\frac{\partial u}{\partial x} - \frac{2}{3}\mu\left(\frac{\partial u}{\partial x} + \frac{\partial v}{\partial y}\right)\right] - \frac{\partial}{\partial y}\left[\mu\left(\frac{\partial u}{\partial y} + \frac{\partial v}{\partial x}\right)\right] = 0 \tag{2}$$

$$\frac{\partial(\rho uv)}{\partial x} + \frac{\partial(\rho vv)}{\partial y} + \frac{\partial p}{\partial y} - \frac{\partial}{\partial x}\left[\mu\left(\frac{\partial u}{\partial y} + \frac{\partial v}{\partial x}\right)\right] - \frac{\partial}{\partial y}\left[2\mu\frac{\partial v}{\partial y} - \frac{2}{3}\mu\left(\frac{\partial u}{\partial x} + \frac{\partial v}{\partial y}\right)\right] = 0 \tag{3}$$

Energy:

$$\frac{\partial(\rho uh)}{\partial x} + \frac{\partial(\rho vh)}{\partial y} + \frac{\partial}{\partial x}\left(\rho\sum_{k=1}^{K_g} Y_k h_k V_{k,x} - \lambda_g\frac{\partial T}{\partial x}\right) + \frac{\partial}{\partial y}\left(\rho\sum_{k=1}^{K_g} Y_k h_k V_{k,y} - \lambda_g\frac{\partial T}{\partial y}\right) = 0 \tag{4}$$

Gas-phase species:

$$\frac{\partial(\rho uY_k)}{\partial x} + \frac{\partial(\rho vY_k)}{\partial y} + \frac{\partial}{\partial x}(\rho Y_k V_{k,x}) + \frac{\partial}{\partial y}(\rho Y_k V_{k,y}) - \dot{\omega}_k W_k = 0 \qquad k = 1, 2...K_g \tag{5}$$

Surface species:

$$\frac{\partial\theta_m}{\partial t} - \frac{1}{\Gamma}\sigma_m\dot{s}_m = 0 \qquad m = 1, 2...K_s \tag{6}$$

The $\partial\theta_m/\theta t$ in eq 6 did not represent an actual transient term but only assisted convergence of the surface coverage algebraic system of equations, which was solved with a Newton method.[37] The diffusion velocities $V_{k,x}$ and $V_{k,y}$ were evaluated by means of a mixture-average model augmented with thermal diffusion[38] for the light species H_2 and H:

$$\vec{V}_k = -D_{km}\vec{\nabla}\left(\ln\frac{Y_k\bar{W}}{W_k}\right) - \frac{D_k^T W_k}{\rho Y_k\bar{W}}\vec{\nabla}(\ln T) \qquad k = 1, 2, ...K_g \tag{7}$$

DOI: 10.1021/acs.energyfuels.7b02011
Energy Fuels 2017, 31, 11448−11459

Finally, the ideal gas and caloric equations of state were:

$$p = \rho \frac{R^0}{\overline{W}} T \quad \text{and} \quad h_k = h_k^0(T_0) + \int_{T_0}^{T} c_{p,k}\, \mathrm{d}T$$
$$k = 1, 2, \ldots K_g \tag{8}$$

At the lower and upper walls ($y = 0$ and $y = 2b$, respectively) the gaseous species and energy boundary conditions were:

$$-(\rho Y_k V_{k,y})_{y=0} + \dot{s}_k W_k = 0 \quad \text{and}$$
$$(\rho Y_k V_{k,y})_{y=2b} + \dot{s}_k W_k = 0 \qquad k = 1, 2, \ldots K_g \tag{9}$$

$$T(x, y = 0) = T_{w,\mathrm{LOW}}(x) \quad \text{and}$$
$$T(x, y = 2b) = T_{w,\mathrm{UP}}(x) \tag{10}$$

where $T_{w,\mathrm{LOW}}(x)$ and $T_{w,\mathrm{UP}}(x)$ were the thermocouple-measured axial profiles of temperature for the lower and upper catalytic walls.

Following the simulation of the experimental conditions, a detailed parametric numerical study was conducted for planar channels with heights $2b$ up to 60 mm and corresponding lengths up to a few meters. The very large channel domains, in conjunction with the required massive number of simulations, precluded the use of a NS solver. A computationally tractable boundary layer (BL) model was used instead. The BL solver allowed for an axially marching solution, which negated the computationally intensive iterative solution of the NS solver and allowed for efficient calculations irrespective of the channel length. The latest version of the BL code along with the governing equations has been described elsewhere.[39]

The applicability of the BL model in reactive channel flows has been assessed for pure heterogeneous combustion in Raja et al.[40] and for combined hetero/homogeneous combustion in Mantzaras et al.[41] It was shown[40] that for sole heterogeneous combustion the BL approximation was valid even for inlet Reynolds numbers as low as 50—values much lower than those of the present work. However, the prediction of gaseous ignition and of the resulting flame shapes in combined hetero/homogeneous combustion introduced more stringent limits: BL models were only suitable for inlet velocities larger than a lower limit that depended on the laminar burning rate of the inlet gaseous mixture.[41] It will be shown in Section 4.3 that the lean $H_2/O_2/N_2$ mixtures posed no restriction on the applicability of the BL code when homogeneous combustion was present. Finally, the elevated surface temperatures in the BL parametric studies allowed for a laminar flow model. It was shown[42,43] that the intense flow laminarization arising from the hot walls guaranteed laminar flows for inlet Reynolds numbers even in excess of 10 000 provided that the wall temperatures were higher than 1100 K.

The detailed H_2/O_2 surface reaction mechanism on platinum from Deutschmann et al.[25] was used, with 14 reactions, 6 gaseous and 5 surface species, and a site density $\Gamma = 2.7 \times 10^{-9}$ mol/cm^2; the surface species were H(s), OH(s), O(s), H_2O(s), Pt(s), and the gaseous species were H_2, O_2, H_2O, OH, H, and O. The elementary gaseous mechanism by Burke et al.[29] was additionally used, having 21 reversible reactions and nine species: H_2, O_2, O, H, OH, H_2O, HO_2, H_2O_2, and N_2. This mechanism, while specifically designed to improve the high-pressure and low-temperature behavior, retained a good performance in the pressure range of interest (1.0−3.5 bar) as manifested with comparisons against ignition delay, laminar burning rate, and species profile measurements.[29] Gas-phase and catalytic chemical rates have been calculated using Chemkin[44] and surface-Chemkin,[45] respectively, while all transport data have been evaluated from the Chemkin database.[38]

4. RESULTS AND DISCUSSION

4.1. Comparison of Simulations and Measurements. Simulated (using the NS code) and measured two-dimensional maps of the OH radical are shown in Figure 2. For all cases with vigorous homogeneous combustion, two flame branches parallel to the catalyst surfaces were formed. This was an outcome of the low Lewis number of hydrogen ($Le_{H2} \sim 0.3$): hydrogen was transported much faster from the center of the channel toward the catalytic surfaces than heat was transported away from the hot catalytic surfaces to the overlying gas, thus restraining the gaseous combustion into narrow zones parallel to the hot walls.[20] This was in strong contrast to H_2/air hetero/homogeneous combustion at rich stoichiometries, where the limiting O_2 reactant had a Lewis number larger than unity ($Le_{O2} \sim 2.0$), leading to contiguous flames spanning the entire channel height.[46,47]

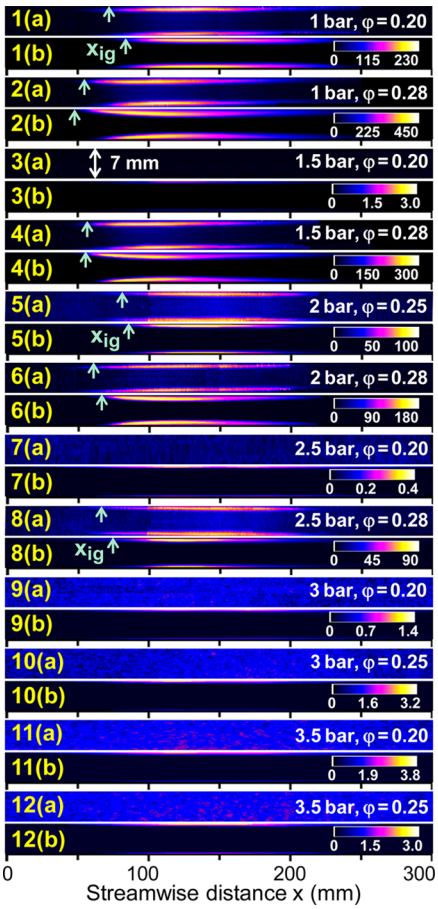

Figure 2. (a) LIF-measured and (b) numerically predicted 2-D maps of OH for all cases in Table 1. Vertical arrows marked x_{ig} define the locations of homogeneous ignition. The scales in the color bars span the minimum and maximum predicted OH in ppmv.

Measurements and predictions in Figure 2 were in good agreement with each other, regarding the homogeneous ignition locations and the resulting shapes of the flames.

DOI: 10.1021/acs.energyfuels.7b02011
Energy Fuels 2017, 31, 11448−11459

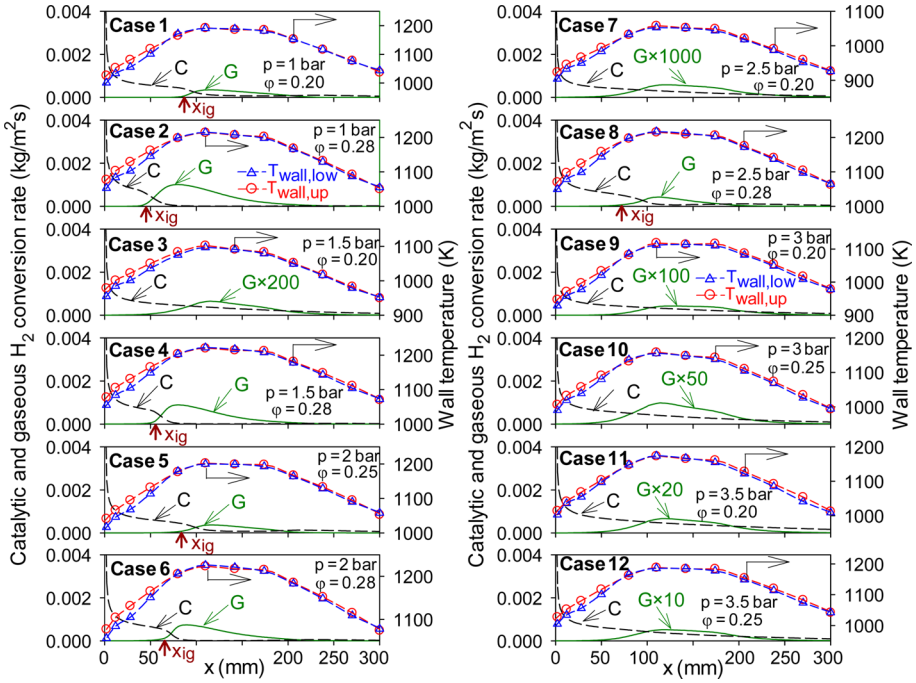

Figure 3. Computed streamwise profiles of catalytic (C, dashed lines) and gaseous (G, solid lines) hydrogen conversion rates for all cases in Table 1. Measured wall temperatures (upper wall: circles; lower wall: triangles) and fitted temperature profiles through the thermocouples are also shown. Vertical arrows marked x_{ig} denote the homogeneous ignition locations.

Gaseous ignition was designated by the arrows marked x_{ig} in Figure 2, determined in either simulations or measurements as the most upstream axial positions where OH attained 5% of its peak value inside the whole channel. Discrepancies between simulated and measured x_{ig} were modest, extending from 3.5% to 15.0%. For $p > 2.5$ bar gas-phase combustion was not ignited, as evidenced by the absence of appreciable OH signals in the LIF measurements and the corresponding very low computed OH levels (up to 3.8 ppmv); such low OH concentrations were in turn not adequate for the planar LIF technique. For pressures below 2.5 bar flames were established in most cases, with the exception of Case 3 at 1.5 bar and Case 7 at 2.5 bar. This was due to their lowest equivalence ratio φ = 0.20 and their lower wall temperatures (mean wall temperatures $T_{w,m}$ = 1030 K for Case 3 and $T_{w,m}$ = 990 K for Case 7), while at the same corresponding pressures Cases 4 and 8 had higher φ (= 0.28) and higher $T_{w,m}$ (= 1150 and 1143 K, respectively). In addition, Case 3 had the highest N_2 dilution among all cases (see Table 1). The simulations have also captured the lack of homogeneous combustion in Cases 3, 7, and 9−12.

The light blue backgrounds in the LIF measurements at the higher pressures (Cases 9−12 in Figure 2, without gaseous combustion) designated higher levels of noise, which became more pronounced as the gain of the CCD camera was increased in an attempt to observe the diminishing OH. The reason for the dwindling homogeneous combustion at elevated pressures will be elaborated in Section 4.2. Finally, for all cases with vigorous gaseous combustion the formed flames were slightly asymmetric (see Figure 2) as a result of the small variations between the lower and the upper surface temperatures, which were typically less than 30 K (see the measured wall temperature profiles in Figure 3).

Axial profiles of the computed hydrogen catalytic conversion rates (C, accounting for both catalytic walls) and gaseous conversion rates (G, integrated over the entire 7 mm height of the channel) as well as the measured temperatures at both walls are given in Figure 3. In all homogeneously ignited cases, the predicted x_{ig} locations (defined by the 5% OH rise) have also been included. It was evident that the rise of the OH radicals matched the rise of the G rates. For the nonignited cases in Figure 2, a minute gas-phase hydrogen conversion was present as shown by the G profiles in Figure 3, which for clarity have been multiplied by factors of 10−1000.

The agreement between measured and predicted x_{ig} in Figure 2 (or in the same manner the agreement in the lack of homogeneous combustion) could not by itself guarantee the validity of the employed gaseous reaction mechanism, as there existed infinite pairs of heterogeneous and homogeneous chemical reactivities leading to the same gas-phase ignition distances.[48] Thus, to ensure against falsification of gaseous kinetics, the heterogeneous processes upstream of gaseous ignition ($0 < x < x_{ig}$) ought to be correctly captured by the model. For the present conditions, the limiting reactant reached transport-limited catalytic conversion, as demonstrated by the almost zero predicted H_2 at the upper and lower walls (see Figure 4). The Raman measurements in Figure 4 captured this trend, notwithstanding the absence of measuring points within 0.7 mm from the catalytic walls. Then measured H_2 and H_2O mole fraction transverse profiles for Cases 6 and 10 (Figure 4) agreed very well with the corresponding predictions. All comparisons between Raman measurements and predictions in Figure 4 referred to axial positions preceding homogeneous ignition. Case 6 had a measured homogeneous ignition distance x_{ig} = 63 mm, with the two selected axial locations being x = 21 and 51 mm. On the other hand, in Case 10 gas-phase combustion was not ignited; hence comparisons between Raman measurements and simulations have been presented down to x = 96 mm.

DOI: 10.1021/acs.energyfuels.7b02011
Energy Fuels 2017, 31, 11448−11459

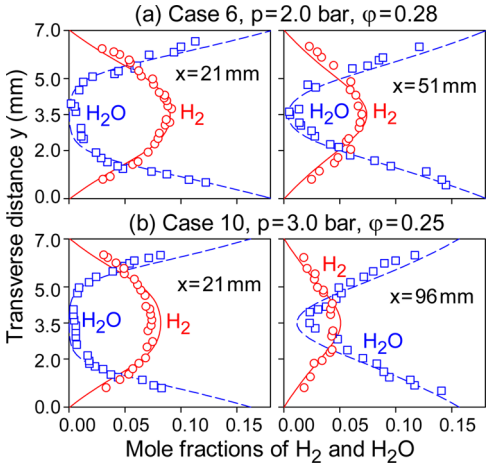

Figure 4. Raman-measured (symbols) and predicted (lines) transverse profiles of H_2 (circles and solid lines) and H_2O (squares and dashed lines) mole fractions, for (a) Case 6 at x = 21 and 51 mm, and (b) Case 10 at x = 21 and 96 mm.

4.2. Pressure Dependence of Homogeneous Ignition.

As discussed in the foregoing section, for all cases with $p \geq 3$ bar, homogeneous combustion was overall inhibited. This behavior reflected the joint effects of intrinsic homogeneous kinetics of hydrogen, which were strongly pressure dependent as discussed next, and of the hetero/homogeneous chemical pathway coupling. This coupling primarily originated from the preceding catalytic combustion over the gaseous induction zone ($0 < x < x_{ig}$) that consumed hydrogen at the expense of the homogeneous pathway and also from the heterogeneously produced H_2O that acted as an effective collision partner in the gas-phase chain terminating reaction $H + O_2 + M \leftrightarrow HO_2 + M$.[20,21] On the contrary, the coupling of the homogeneous and homogeneous pathways through radical adsorption and desorption reactions was modest.[20,21]

To understand the pressure dependence of homogeneous ignition, initially the intrinsic gas-phase ignition characteristics (without including catalytic chemistry) of lean H_2/air mixtures were studied numerically. Gas-phase ignition delays, τ_{ig}, have been calculated in a batch reactor at constant pressure using the Senkin code of Chemkin.[49] Plots of τ_{ig} as a function of pressure are illustrated in Figure 5 for different initial temperatures and two equivalence ratios φ = 0.1 and 0.3. Ignition delays have been determined as the inflection points in the temperature versus time histories.

The initial (t = 0) batch reactor temperatures in Figure 5 were selected to mimic the temperatures in the experiments. In the spatially inhomogeneous channel-flow reactor, the wall temperatures in the gaseous induction zones ($0 < x < x_{ig}$) could be considered as representative for gas-phase ignition, since the effect of inlet temperature was typically weak.[20] Using only the temperatures at the wall and neglecting the temperatures at the inlet, a higher limit for the characteristic temperatures of all homogeneously ignited cases was 1000−1175 K (by including a 10% weight for the inlet temperature, this range dropped to 910−1090 K). For the nonignited cases, a similar wall temperature range (965−1188 K) was obtained when considering the spatial extent down to the peak position of the minute G conversion profiles in Figure 3. To facilitate the forthcoming discussion, the temperatures in the ignition delay simulations of Figure 5 encompassed the aforementioned

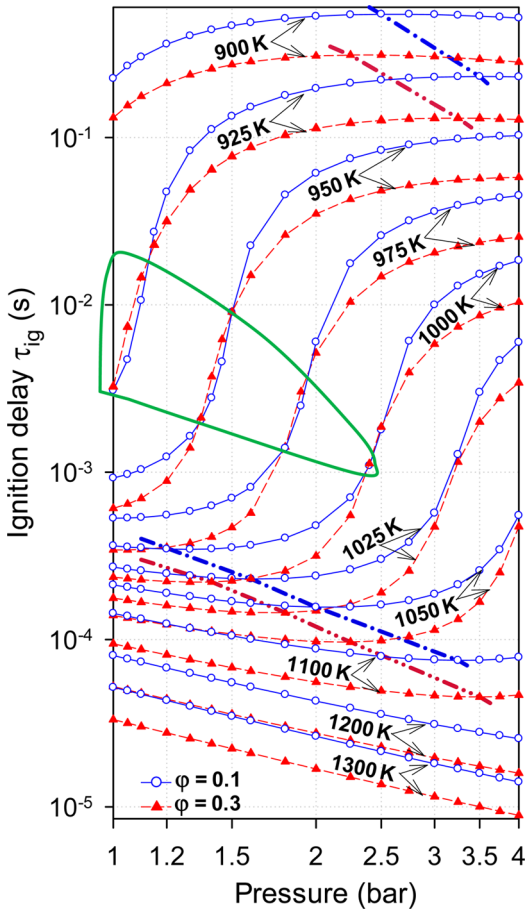

Figure 5. Ignition delays of H_2/air mixtures for φ = 0.1 (open circles and solid lines) and 0.3 (filled triangles and dashed lines) in a constant pressure batch reactor, as a function of pressure and initial temperature. Thick dashed−dotted and dashed−double-dotted lines denote the minima and maxima of the ignition delay times for φ = 0.1 and 0.3, respectively. The circled area demarcates conditions where the ignition delays at φ = 0.1 are shorter than those at φ = 0.3.

measured wall temperatures, covering the wider range 900−1300 K.

Figure 5 indicated a strong pressure dependence of the ignition delays, especially for T < 1050 K. Characteristically, at 1000 K and φ = 0.1 the ratio of the longest ignition delay (p = 3.5 bar) to the shortest one (p = 1.2 bar) was 43, while for φ = 0.3 the corresponding ratio was 39. On the other hand, at pressures above 4 bar and until 15 bar, a modest pressure dependence of the ignition delays for T < 1050 K has been shown.[21] The strong ignition delay dependence at the low pressures 1.0−3.5 bar and modest temperatures of catalytic systems justified the present detailed hetero/homogeneous studies at pressures up to 3.5 bar.

For the pressure range 1.0−3.5 bar and for initial temperatures 950−975 K in Figure 5, the ignition delays increased (the gaseous reactivity decreased) sharply with rising pressure especially between 1.0 and 2.0 bar. Conversely, for the highest range of initial temperatures 1200−1300 K, the ignition delays decreased (i.e., the homogeneous reactivity was amplified) with increasing pressure. In the temperature ranges 900−925 K and 1000−1100 K, the homogeneous reactivity exhibited a more complicated and nonmonotonic behavior. For 1000−1100 K the ignition delays decreased until a critical pressure, above which the ignition delays increased, while for

DOI: 10.1021/acs.energyfuels.7b02011
Energy Fuels 2017, 31, 11448−11459

900−925 K the gaseous ignition delays first increased and then decreased above a critical pressure. The upper and lower critical pressures are shown with thick lines in Figure 5. This complex behavior mirrored the second explosion limit as well as the extended second explosion limit of H_2 and was a result of the competition among: (a) the chain-branching step $H + O_2 \leftrightarrow O + OH$, (b) the chain-terminating step $H + O_2 + M \leftrightarrow HO_2 + M$, and (c) the chain-branching steps $HO_2 + H_2 \leftrightarrow H_2O_2 + H$ and $H_2O_2 + M \leftrightarrow 2OH + M$ which became significant at higher temperatures.[46,50] The elongated ignition delays above a pressure of ca. 2.5−3.0 bar for $T \leq 1025$ K were mainly responsible for the suppression of gaseous combustion at 3.0 and 3.5 bar in Figure 2, as discussed next.

For a noncatalytic channel with the same wall temperatures as in the catalytic channel (see Figure 3), the elongated gas-phase ignition delays above ∼2.5 bar would only affect the location of homogeneous ignition but would not suppress gaseous combustion, provided that the residence times (dictated by the 300 mm channel length and the inflow velocities in Table 1) were sufficiently long. However, for catalytic channels the elongated ignition delays allowed for enhanced catalytic hydrogen consumption such that gaseous combustion could be effectively suppressed, irrespective of residence time. It is pointed out that the heterogeneous pathway was a strong competitor to the gaseous pathway in consuming hydrogen for two reasons: its high molecular transport and its high catalytic reactivity on platinum. Finally, while Figure 5 referred to gaseous combustion alone, in hetero/homogeneous combustion the catalytically generated H_2O during the gaseous induction zone would further inhibit gas-phase ignition[19,20] owing to the large water third body efficiency in $H + O_2 + M \leftrightarrow HO_2 + M$. The aforementioned inhibition becomes, in turn, stronger at elevated pressures.[21]

The above results have shown a very complex behavior of the homogeneous ignition processes during hetero/homogeneous combustion of lean H_2/air mixtures at pressures 1.0−3.5 bar. Implications of these findings to practical systems operating in this pressure range (microreactors and recombiners) are addressed in the coming section.

4.3. Homogeneous Combustion Regimes. The experimental and numerical results in Figures 2 and 4 have established the validity of the employed heterogeneous and homogeneous reaction mechanisms. Following this validation, a detailed parametric numerical study has been performed to map the regimes where homogeneous combustion was important in channels coated with platinum. To this direction, the operating parameters were varied in the following ranges: pressure $p = 1.0-3.5$ bar, wall temperature $T_w = 1000-1400$ K, and inlet velocity $U_{IN} = 0.5-3.0$ m/s referring to $p = 1$ bar; at higher pressures U_{IN} were scaled down to have the same mass flow rates ($2b\rho_{IN}U_{IN}$). Two stoichiometries were examined ($\varphi = 0.1$ and 0.3) with a common $T_{IN} = 300$ K. Homogeneous combustion strongly depended on the geometrical confinement (surface-to-volume ratio or channel height) as it determined the relative consumption of hydrogen due to the surface heterogeneous pathway and the volumetric homogeneous pathway. Analytical studies based on activation energy asymptotics[51] have shown that homogeneous ignition in catalytic channels was promoted by increasing the channel height $2b$, such that x_{ig} was a monotonically decreasing function of $2b$.

Simulations were performed by successively increasing the channel height $2b$ to the value needed for achieving a gaseous hydrogen conversion amounting to 5% of the entire (heterogeneous and homogeneous) hydrogen consumption in the channel. In other words, the requirement was $\int_{x=0}^{x=L} G\, dx / \int_{x=0}^{x=L} (C + G)\, dx = 0.05$ with C and G the local catalytic and gaseous hydrogen conversions (see e.g. Figure 3). The maximum investigated channel height was $2b = 60$ mm, as it far-exceeded typical sizes of microreactors and nuclear recombiners.[5,52] In all computations, the channel length was adjusted (depending on the height $2b$ and U_{IN}) so as to ensure at least 99.5% hydrogen conversion at the channel exit when using only catalytic chemistry in the simulations. This procedure guaranteed that the potential absence of gaseous combustion was solely due to chemical reasons (either due to intrinsic gaseous chemistry or due to hetero/homogeneous chemistry interactions) and not due to insufficient residence times for the onset of homogeneous ignition. The minimum channel height $2b$ yielding 5% gaseous conversion will be henceforth termed critical height H_{cr}. Simulations with refined channel heights yielded 2% accuracy for the computed H_{cr}. The height refinement procedure and the overall large channel sizes necessitated, as discussed in Section 3, the use of a computationally efficient boundary layer (BL) code.

The requirements for the applicability of the BL approximation in the presence of gaseous combustion have been laid down in ref 41. As BL models lack axial diffusion, a cardinal requirement for their validity is the establishment of flames inside the channel having shallow sweep angles (the acute angle defined by the flame and the x-direction) so as to minimize the axial diffusion induced by the steep gradients in the flame-normal direction. The flame sweep angle was in turn largely controlled by the relative magnitude of U_{IN} and the laminar flame speed S_L of the gaseous mixture. Criteria for the BL applicability were presented for the case of CH_4/air hetero/homogeneous combustion in.[41] Hydrogen at lean stoichiometries in air was ideally suited for the applicability of the BL model, due to the formation of flames nearly parallel to the catalytic walls (see Figure 2), that is, with practically zero flame sweep angles. This is further demonstrated in Figure 6,

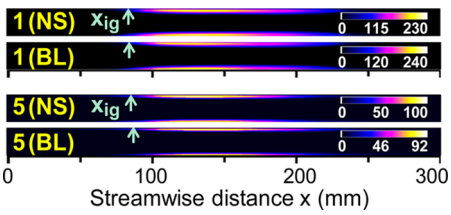

Figure 6. Predicted 2-D OH maps for Cases 1 and 5 using the Navier−Stokes (NS) and boundary layer (BL) codes. Vertical arrows marked x_{ig} denote the homogeneous ignition positions. The provided scales in the color bars span the minimum and maximum predicted OH in ppmv.

providing comparisons between NS and BL predictions for Cases 1 and 5 in Table 1; it is evident that the homogeneous ignition distances and flame shapes of the two simulations practically coincided.

Critical channel heights H_{cr} versus inlet velocity are plotted in Figure 7 ($\varphi = 0.1$) and Figure 8 ($\varphi = 0.3$) with parameters pressure ($p = 1.0-3.5$ bar) and wall temperature ($T_w = 1100-1400$ K). For the still lower $T_w = 1000$ K, there was no appreciable gas-phase hydrogen conversion even for channels with heights up to the maximum investigated 60 mm. In all

DOI: 10.1021/acs.energyfuels.7b02011
Energy Fuels 2017, 31, 11448−11459

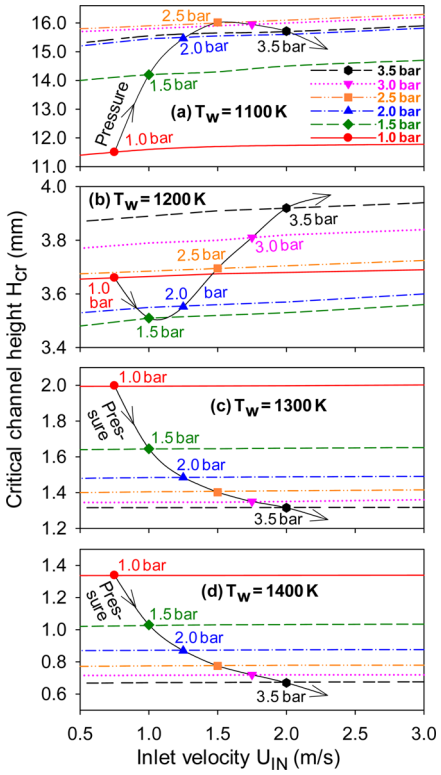

Figure 7. Computed critical heights H_{cr} in a planar Pt-coated channel as a function of inlet velocity U_{IN}, for various wall temperatures T_w and p = 1.0−3.5 bar. Solid lines with arrows denote the direction of H_{cr} variation with increasing pressure. H_2/air mixture at φ = 0.1, T_{IN} = 300 K. The U_{IN} scale refers to p_0 = 1 bar; for higher pressures $U_{IN,p} = U_{IN,po}(p_0/p)$.

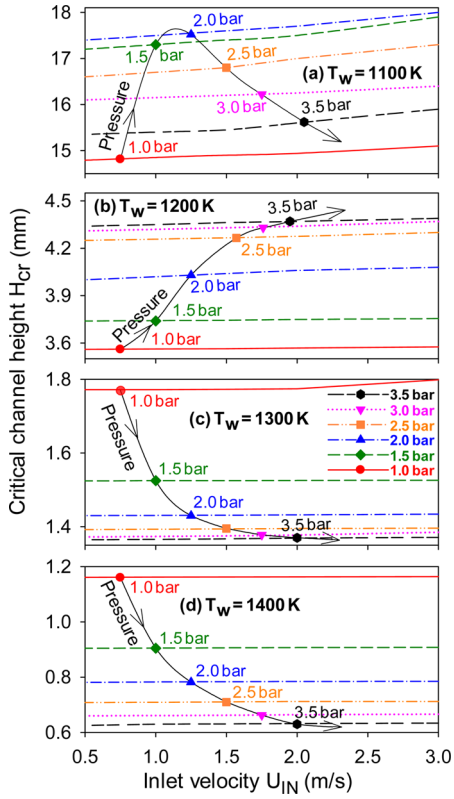

Figure 8. Computed critical heights H_{cr} in a planar Pt-coated channel as a function of inlet velocity U_{IN}, for various wall temperatures T_w and p = 1.0−3.5 bar. Solid lines with arrows denote the direction of H_{cr} variation with increasing pressure. H_2/air mixture at φ = 0.3, T_{IN} = 300 K. The U_{IN} scale refers to p_0 = 1 bar; for higher pressures $U_{IN,p} = U_{IN,po}(p_0/p)$.

cases, the dependence on U_{IN} was weak, with H_{cr} increasing only modestly with rising inlet velocity. For the high wall temperatures T_w = 1300 and 1400 K, H_{cr} dropped monotonically with increasing pressure for both φ (see Figure 7c, d and Figure 8c, d), indicating the promotion of homogeneous combustion with rising pressure. This was in qualitative agreement with the shorter ignition delays at higher pressures shown in Figure 5 for 1300 K. Catalytic microreactors for small-scale portable power generation had typical channel hydraulic diameters of less than 2 mm,[5,53] implying that for T_w = 1300−1400 K gaseous combustion could not be neglected. For such temperatures and especially for microturbine-based small power generation systems designed for operation at 3−4 bar,[54] there could be appreciable gaseous combustion in the catalytic reactor. On the other hand, catalytic hydrogen recombiners comprised noble-metal-coated flat metallic plates at a separation (or effective channel height) of about 1 cm.[52] This configuration was much more prone to vigorous homogeneous combustion at T_w = 1300−1400 K, since H_{cr} was always much smaller than 1 cm (0.62−1.34 mm).

For the lowest wall temperature T_w = 1100 K the H_{cr} was nonmonotonically dependent on pressure for both equivalence ratios (see Figures 7aand 8a), with H_{cr} initially rising with increasing pressure until 2.0−2.5 bar and then dropping with rising pressure. This qualitatively agreed with the ignition delay plots (Figure 5) for the lowest temperatures of 900 or 925 K. The temperature disparity between the 0-D ignition delay calculations and the 2-D channel simulations was, as discussed before, due to the lack of a uniquely defined temperature in the spatially inhomogeneous channel. For channels with heights $2b$ < 11 mm, gas-phase combustion was altogether suppressed at T_w = 1100 K, irrespective of pressure or equivalence ratio. This implied that for catalytic microreactors in small-scale portable power generation ($2b \leq 2$ mm) a wall temperature of T_w = 1100 K (or less) fully negated gaseous combustion. Only for the larger channels employed in catalytic recombiners homogeneous combustion could become relevant at T_w = 1100 K. Furthermore, pressures of 2.0−2.5 bar were the most effective in mitigating gaseous combustion at T_w = 1100 K as they resulted in the largest H_{cr} (∼15−18 mm).

While for T_w = 1300 and 1400 K the computed H_{cr} were always smaller at φ = 0.3 than φ = 0.1 (in agreement with Figure 5 showing at 1300 K higher gas-phase reactivity of hydrogen at φ = 0.3), this trend was reversed for T_w = 1100 and 1200 K. In particular, for low pressures the computed H_{cr} were smaller for φ = 0.1 compared to φ = 0.3, while this difference diminished with increasing pressure. This can be seen in Figure 9, providing H_{cr} for the two equivalence ratios as a function of pressure at T_w = 1100 K and U_{IN} = 2 m/s. The lower pressure behavior in Figure 9 could be explained from the ignition delay plots in Figure 5 at 925−975 K. Therein, the two equivalence ratio plots crossed in the range 1.0 bar < p < 2.0 bar, leading to shorter ignition delays at φ = 0.1 than φ = 0.3 (see circled zone in Figure 5). Hence, the behavior in Figure 9 at p = 3.5 bar (slightly smaller H_{cr} at φ = 0.3) was in agreement to Figure 5. Only the p = 3 bar results in Figure 9 (smaller H_{cr} at φ = 0.1) could not be readily explained from Figure 5. However, it should be noted that in the spatially inhomogeneous channel

DOI: 10.1021/acs.energyfuels.7b02011
Energy Fuels 2017, 31, 11448−11459

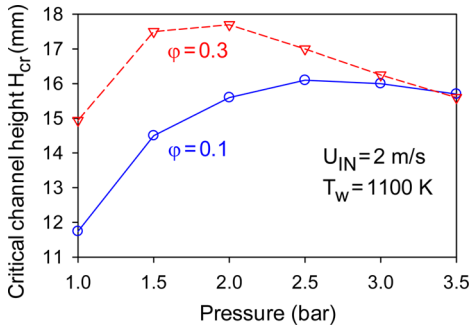

Figure 9. Computed critical channel heights H_{cr} as a function of pressure for φ = 0.1 and 0.3, inlet velocity U_{IN} = 2 m/s, and wall temperature T_w = 1100 K. The U_{IN} = 2 m/s refers to p_0 = 1 bar; for higher pressures $U_{IN,p} = U_{IN,po}(p_0/p)$.

the equivalence ratio dropped significantly along the streamwise distance due to the ongoing catalytic consumption of hydrogen. The drop in equivalence ratio is demonstrated in Figure 10,

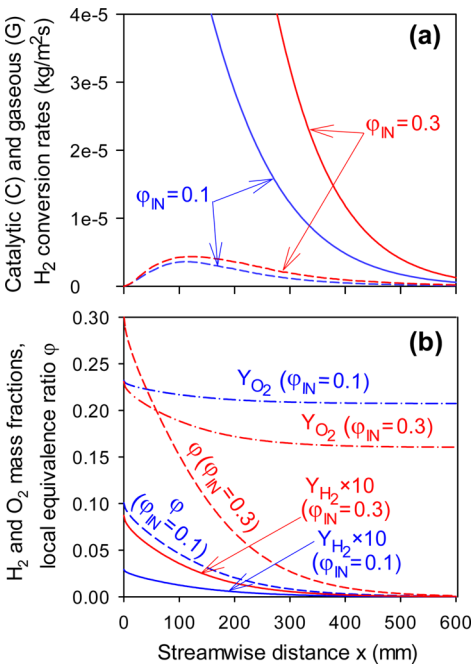

Figure 10. (a) Computed streamwise profiles of: (a) catalytic (C) and gaseous (G) hydrogen conversion rates for inlet φ = 0.1 and 0.3, (b) H_2 and O_2 mass fractions and local equivalence ratios. Channel height of 11.6 mm (H_{cr} for φ = 0.1), U_{IN} = 1 m/s, p = 1 bar, T_w = 1100 K.

providing axial profiles of hydrogen catalytic (C) and gaseous (G) conversion rates (Figure 10a) for two cases with inlet φ = 0.1 and 0.3 and T_w = 1100 K,and transversely averaged streamwise profiles of H_2 and O_2 mass fractions and of the local equivalence ratios (Figure 10b). The simulations in Figure 10 refer to a channel height of 11.6 mm (critical height H_{cr} for φ = 0.1). It was evident that the local equivalence ratio dropped significantly over the axial extent of the gaseous (G) conversion and this in turn may have crucially affected the pressure ranges of crossing between the equivalence ratio plots (circled area in Figure 5).

Details of the heterogeneous and homogeneous combustion processes are finally discussed in Figure 11. Two-dimensional distributions of OH are shown over half the channel domain

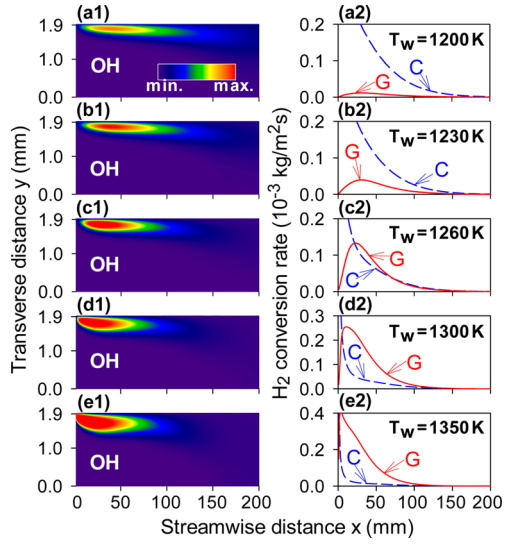

Figure 11. (a1−e1) Computed 2-D maps of OH for a channel with height $2b$ = 3.84 mm, φ = 0.1, p = 3 bar, U_{IN} = 1 m/s, and wall temperatures T_w = 1200−1350. Half of the domain is shown (y = 0 is the symmetry plane and y = 1.92 mm the gas/wall interface). The color bar identifies the OH minima and maxima. The minima are 0, and the maxima (ppmv) are (a1) 5.9, (b1) 20, (c1) 74, (d1) 152, and (e1) 247. (a2−e2) Transverse profiles of catalytic (C) and gaseous (G) hydrogen conversion rates for the same cases as in a1−e1.

(Figure 11a1−e1) as well as axial profiles of hydrogen conversions (Figure 11a2−e2) for p = 3 bar, U_{IN} = 1 m/s, φ = 0.1, and wall temperatures T_w = 1200−1350 K. The channel height was $2b$ = 3.84 mm (critical H_{cr} for T_w = 1200 K). In all cases homogeneous ignition was attained in the vicinity of the channel entry; nonetheless, the contribution of gaseous chemistry diminished with dropping T_w as manifested by the relative magnitudes of the C and G plots in Figure 11a2−e2. Catalytic and gaseous combustion coexisted, as evidenced by the spatial overlap of the C and G conversions. At the lower wall temperatures, there was substantial H_2 leakage through the homogeneous combustion zone, and the escaping hydrogen was afterward consumed heterogeneously at the channel walls. This was a result of the weaker flames formed at lower wall temperatures which, due to their longer flame transit times, could not fully consume the transverse hydrogen fluxes transported from the channel core (y = 0) to the channel wall (y = 1.92 mm). On the other hand, for the highest T_w = 1350 K, the formed flames were stronger (with appreciably shorter flame transit times) leading to a much smaller leakage across the homogeneous combustion zones and hence to a much lower heterogeneous C consumption (Figure 11e2).

5. CONCLUSIONS

One-dimensional Raman measurements of major gaseous species concentrations and planar laser-induced fluorescence of the hydroxyl radical were applied in a platinum-coated channel to investigate the hetero/homogeneous combustion of lean H_2/air mixtures (φ = 0.20−0.28) at pressures 1.0−3.5 bar. This pressure range was of particular interest for microreactors used in portable power generation and also for catalytic hydrogen recombiners of nuclear power plants. The experiments were simulated with a 2-D Navier−Stokes code that included elementary homogeneous and detailed heterogeneous reaction mechanisms. Elaborate numerical parametric studies

DOI: 10.1021/acs.energyfuels.7b02011
Energy Fuels 2017, 31, 11448−11459

were further performed, using a boundary layer code, to delineate the operating regimes (pressure, wall temperature, inlet velocity, equivalence ratio) and geometrical confinement (critical channel heights) allowing for appreciable gaseous combustion. The key conclusions are as follows.

(1) The used heterogeneous and homogeneous chemical mechanisms captured the measured locations of gas-phase ignition as well as the ensuing flame shapes at pressures up to 2.5 bar. The LIF measurements demonstrated suppression of gaseous combustion above 2.5 bar, a behavior also captured by the model. Moreover, transport-limited heterogeneous hydrogen conversion was confirmed by both numerical simulations and measurements.

(2) Gaseous combustion was controlled by the intricate pressure dependency of gaseous ignition chemistry and also by the competition between the catalytic and gaseous chemical pathways. Over the investigated average channel wall temperatures ∼1000−1100 K, the homogeneous ignition chemistry exhibited nonmonotonic pressure dependence such that above a critical pressure homogeneous ignition was inhibited (the ignition delay times were longer). Above the critical pressures the catalytic pathway competed effectively with the gaseous pathway for the consumption of hydrogen, resulting in an overall suppression of gaseous combustion in the range 2.5 bar $< p \leq 3.5$ bar.

(3) For lean H_2/air mixtures, gas-phase ignition led to the formation of two flame branches extending parallel to the channel walls. This behavior minimized strong axial gradients and allowed for accurate modeling of the homogeneous combustion processes using a computationally efficient boundary layer code as opposed to a full Navier−Stokes code.

(4) Extensive parametric studies were carried out using the boundary layer code by varying the channel heights ($2b$ = 0.5−60 mm), pressures (p = 1.0−3.5 bar), wall temperatures (T_w = 1000−1400 K), and inlet velocities (U_{IN} = 0.5−3.0 m/s). The critical channel heights H_{cr}, above which gaseous combustion accounted for more than 5% of the total hydrogen conversion, were assessed for H_2/air equivalence ratios φ = 0.1 and 0.3. For T_w = 1000 K, gaseous combustion was insignificant, even for the largest studied channel height $2b$ = 60 mm. For T_w = 1300 and 1400 K, H_{cr} was a monotonically decreasing function of pressure, while for T_w = 1100 and 1200 K a nonmonotonic dependence of H_{cr} on pressure was obtained.

(5) Implications for practical systems such as catalytic microreactors in portable power generation and catalytic recombiners in nuclear plants were drawn. For catalytic microreactors with typical channel heights less than 2 mm, homogeneous combustion was relevant only for $T_w \geq 1300$ K. Moreover, for such temperatures the homogeneous combustion was always promoted with rising pressure. For hydrogen recombiners with typical channel heights ∼1 cm, homogeneous combustion could become relevant for wall temperatures as low as T_w = 1100 K. For T_w = 1100 K the critical heights H_{cr} exhibited a nonmonotonic pressure dependence. They were largest for p = 2.0−2.5 bar, indicating a safer recombiner operation in this narrow pressure range.

■ AUTHOR INFORMATION

Corresponding Author

*Tel.: +41-56-3104046. Fax: +41-56-3102199. E-mail address: ioannis.mantzaras@psi.ch.

ORCID

Ran Sui: 0000-0003-3758-7506

John Mantzaras: 0000-0002-1039-669X

Notes

The authors declare no competing financial interest.

■ ACKNOWLEDGMENTS

Support by the European Union project HRC-Power is acknowledged. We also thank Mr. J. Theile for helping the experiments.

■ NOMENCLATURE

b = half-height of catalytic channel, eqs 9 and 10
$c_{p,k}$ = heat capacity of k-th gas-phase species, eq 8
D_{km}, D_k^T = mixture-average and thermal diffusion of k-th gas-phase species, eq 7
h = total enthalpy of gas, eq 8
H_{cr} = critical channel height, Figures 7−9
K_g, K_s = total number of gas-phase and surface species, eqs 5 and 6
Le_k = Lewis number of k-th gas-phase species (thermal over mass diffusivity)
p = pressure
$\dot{s}_m$ = catalytic molar production rate of m-th species, eqs 6 and 9
T = temperature of gas, eqs 4, (7) and (8)
u, v = streamwise and transverse velocity components, eqs 1-(5)
U_{IN} = inlet streamwise velocity
W_k, $\bar{W}$ = molecular weight of k-th species, mean gaseous molecular weight, eq 7
x, y = streamwise and transverse channel coordinates, Figure 1
x_{ig} = homogeneous ignition distance, Figures 2 and 3
Y_k = mass fraction of k-th gas-phase species, eq 5

Greek Symbols

Γ = surface site density, eq 6
θ_m = coverage of m-th surface species, eq 6
λ_g = gas thermal conductivity, eq 4
μ = gas dynamic viscosity, eqs 2 and 3
ρ = gas density, eqs 1−5
σ_m = site occupancy of m-th surface species, eq 6
τ_{ig} = ignition delay, Figure 5
φ = hydrogen to oxygen equivalence ratio
$\dot{\omega}_k$ = gaseous molar production rate of k-th gas-phase species, eq 5

Subscripts

IN = inlet
w = wall

Acronyms

SN = signal-to-noise

■ REFERENCES

(1) Hoffmann, S.; Bartlett, M.; Finkenrath, M.; Evulet, A.; Ursin, T. P. Performance and cost analysis of advanced gas turbine cycles with precombustion CO_2 capture. *ASME GT2008−51027*, Berlin, Germany, June 8−13, 2008.

(2) Rubin, E. S.; Mantripragada, H.; Marks, A.; Versteeg, P.; Kitchin, J. The outlook for improved carbon capture technology. *Prog. Energy Combust. Sci.* **2012**, *38* (5), 630−671.

(3) Bolaños, F.; Winkler, D.; Piringer, F.; Griffin, T.; Bombach, R.; Mantzaras, J. Study of a rich/lean staged combustion concept for

DOI: 10.1021/acs.energyfuels.7b02011
Energy Fuels 2017, 31, 11448−11459

hydrogen at gas turbine relevant conditions. *ASME GT2013−94420*, San Antonio Texas, USA, June 3−7, 2013.
(4) Norton, D. G.; Wetzel, E. D.; Vlachos, D. G. Fabrication of single-channel catalytic microburners: effect of confinement on the oxidation of hydrogen/air mixtures. *Ind. Eng. Chem. Res.* **2004**, *43*, 4833−4840.
(5) Sui, R.; Prasianakis, N. I.; Mantzaras, J.; Mallya, N.; Theile, J.; Lagrange, D.; Friess, M. An experimental and numerical investigation of the combustion and heat transfer characteristics of hydrogen-fueled catalytic microreactors. *Chem. Eng. Sci.* **2016**, *141*, 214−230.
(6) Seshadri, V.; Kaisare, N. S. Simulation of hydrogen and hydrogen-assisted propane ignition in Pt catalyzed microchannel. *Combust. Flame* **2010**, *157*, 2051−2062.
(7) Sui, R.; Mantzaras, J. Combustion stability and hetero-/homogeneous chemistry interactions for fuel-lean hydrogen/air mixtures in platinum-coated microchannels. *Combust. Flame* **2016**, *173*, 370−386.
(8) Holladay, J. D.; Wang, Y.; Jones, E. Review of developments in portable hydrogen production using microreactor technology. *Chem. Rev.* **2004**, *104*, 4767−4789.
(9) Kaisare, N. S.; Vlachos, D. G. A review on microcombustion: Fundamentals, devices and applications. *Prog. Energy Combust. Sci.* **2012**, *38*, 321−359.
(10) Carroni, R.; Griffin, T.; Mantzaras, J.; Reinke, M. High-pressure experiments and modeling of methane/air catalytic combustion for power generation applications. *Catal. Today* **2003**, *83*, 157−170.
(11) Eriksson, S.; Wolf, M.; Schneider, A.; Mantzaras, J.; Raimondi, F.; Boutonnet, M.; Järas, S. Fuel rich catalytic combustion of methane in zero emissions power generation processes. *Catal. Today* **2006**, *117*, 447−453.
(12) Evans, C. J.; Kyritsis, D. C. Operational regimes of rich methane and propane/oxygen flames in mesoscale non-adiabatic ducts. *Proc. Combust. Inst.* **2009**, *32*, 3107−3114.
(13) Pizza, G.; Frouzakis, C. E.; Mantzaras, J.; Tomboulides, A. G.; Boulouchos, K. Three-dimensional simulations of premixed hydrogen/air flames in microtubes. *J. Fluid Mech.* **2010**, *658*, 463−491.
(14) Pizza, G.; Frouzakis, C. E.; Mantzaras, J. Chaotic dynamics in premixed hydrogen/air channel flow combustion. *Combust. Theory Modell.* **2012**, *16*, 275−299.
(15) Pizza, G.; Mantzaras, J.; Frouzakis, C. E.; Tomboulides, A. G.; Boulouchos, K. Suppression of combustion instabilities of premixed hydrogen/air flames in microchannels using heterogeneous reactions. *Proc. Combust. Inst.* **2009**, *32*, 3051−3058.
(16) Pizza, G.; Mantzaras, J.; Frouzakis, C. E. Flame dynamics in catalytic and non-catalytic mesoscale microreactors. *Catal. Today* **2010**, *155*, 123−130.
(17) Heitsch, M. Fluid dynamic analysis of a catalytic recombiner to remove hydrogen. *Nucl. Eng. Des.* **2000**, *201*, 1−10.
(18) Mantzaras, J., Catalytic Combustion of Hydrogen, Challenges, and Opportunities. In *Modeling and Simulation of Heterogeneous Catalytic Processes, Advances in Chemical Engineering, Vol. 45*, Dixon, A. G., Ed. Elsevier Academic Press Inc: San Diego, USA, 2014; Vol. *45*.
(19) Bui, P. A.; Vlachos, D. G.; Westmoreland, P. R. Homogeneous ignition of hydrogen/air mixtures over platinum. *Symp. Combust., [Proc.]* **1996**, *26*, 1763−1770.
(20) Appel, C.; Mantzaras, J.; Schaeren, R.; Bombach, R.; Inauen, A.; Kaeppeli, B.; Hemmerling, B.; Stampanoni, A. An experimental and numerical investigation of homogeneous ignition in catalytically stabilized combustion of hydrogen/air mixtures over platinum. *Combust. Flame* **2002**, *128*, 340−368.
(21) Ghermay, Y.; Mantzaras, J.; Bombach, R.; Boulouchos, K. Homogeneous combustion of fuel lean $H_2/O_2/N_2$ mixtures over platinum at elevated pressures and preheats. *Combust. Flame* **2011**, *158*, 1491−1506.
(22) Meynet, N.; Bentaib, A.; Giovangigli, V. Impact of oxygen starvation on operation and potential gas-phase ignition of passive auto-catalytic recombiners. *Combust. Flame* **2014**, *161* (8), 2192−2202.
(23) Kraus, P.; Lindstedt, R. P. Reaction class-based frameworks for heterogeneous catalytic systems. *Proc. Combust. Inst.* **2017**, *36*, 4329−4338.
(24) Park, Y. K.; Aghalayam, P.; Vlachos, D. G. A generalized approach for predicting coverage-dependent reaction parameters of complex surface reactions: Application to H_2 oxidation over platinum. *J. Phys. Chem. A* **1999**, *103* (40), 8101−8107.
(25) Deutschmann, O.; Maier, L. I.; Riedel, U.; Stroemman, A. H.; Dibble, R. W. Hydrogen assisted catalytic combustion of methane on platinum. *Catal. Today* **2000**, *59*, 141−150.
(26) Kraus, P.; Frank, I. On the dynamics of H_2 adsorption on the Pt(111) surface. *Int. J. Quantum Chem.* **2017**, *117* (17), e25407.
(27) Ludwig, J.; Vlachos, D. G. Molecular dynamics of hydrogen dissociation on an oxygen covered Pt(111) surface. *J. Chem. Phys.* **2008**, *128* (15), 154708.
(28) Karim, W.; Spreafico, C.; Kleibert, A.; Gobrecht, J.; VandeVondele, J.; Ekinci, Y.; van Bokhoven, J. A. Catalyst support effects on hydrogen spillover. *Nature* **2017**, *541* (7635), 68−71.
(29) Burke, M. P.; Chaos, M.; Ju, Y.; Dryer, F. L.; Klippenstein, S. J. Comprehensive H_2/O_2 kinetic model for high-pressure combustion. *Int. J. Chem. Kinet.* **2012**, *44*, 444−474.
(30) Sanchez, A. L.; Williams, F. A. Recent advances in understanding of flammability characteristics of hydrogen. *Prog. Energy Combust. Sci.* **2014**, *41*, 1−55.
(31) Li, J.; Zhao, Z.; Kazakov, A.; Dryer, F. L. An updated comprehensive kinetic model of hydrogen combustion. *Int. J. Chem. Kinet.* **2004**, *36*, 566−575.
(32) Mantzaras, J.; Bombach, R.; Schaeren, R. Hetero-/homogeneous combustion of hydrogen/air mixtures over platinum at pressures up to 10 bar. *Proc. Combust. Inst.* **2009**, *32*, 1937−1945.
(33) Zheng, X.; Mantzaras, J.; Bombach, R. Homogeneous combustion of fuel-lean syngas mixtures over platinum at elevated pressures and preheats. *Combust. Flame* **2013**, *160*, 155−169.
(34) Reinke, M.; Mantzaras, J.; Schaeren, R.; Bombach, R.; Inauen, A.; Schenker, S. High-pressure catalytic combustion of methane over platinum: in situ experiments and detailed numerical predictions. *Combust. Flame* **2004**, *136*, 217−240.
(35) Sui, R.; Mantzaras, J.; Bombach, R. A comparative experimental and numerical investigation of the heterogeneous and homogeneous combustion characteristics of fuel-rich methane mixtures over rhodium and platinum. *Proc. Combust. Inst.* **2017**, *36*, 4313−4320.
(36) Sui, R.; Mantzaras, J.; Bombach, R.; Denisov, A. Hetero-/homogeneous combustion of fuel-lean methane/oxygen/nitrogen mixtures over rhodium at pressures up to 12 bar. *Proc. Combust. Inst.* **2017**, *36*, 4321−4328.
(37) Dogwiler, U.; Benz, P.; Mantzaras, J. Two-dimensional modelling for catalytically stabilized combustion of a lean methane-air mixture with elementary homogeneous and heterogeneous chemical reactions. *Combust. Flame* **1999**, *116*, 243−258.
(38) Kee, R. J.; Dixon-Lewis, G.; Warnatz, J.; Coltrin, M. E.; Miller, J. A. *A Fortran computer code package for the evaluation of gas-phase multicomponent transport properties*; Peport No. SAND86-8246; Sandia National Laboratories: Albuquerque, 1996.
(39) Zheng, X.; Mantzaras, J. An analytical and numerical investigation of hetero-/homogeneous combustion with deficient reactants having larger than unity Lewis numbers. *Combust. Flame* **2014**, *161*, 1911−1922.
(40) Raja, L. L.; Kee, R. J.; Deutschmann, O.; Warnatz, J.; Schmidt, L. D. A critical evaluation of Navier-Stokes, boundary-layer, and plug-flow models of the flow and chemistry in a catalytic-combustion monolith. *Catal. Today* **2000**, *59*, 47−60.
(41) Mantzaras, J.; Appel, C.; Benz, P. Catalytic combustion of methane/air mixtures over platinum: homogeneous ignition distances in channel flow configurations. *Proc. Combust. Inst.* **2000**, *28*, 1349−1357.
(42) Appel, C.; Mantzaras, J.; Schaeren, R.; Bombach, R.; Inauen, A. Turbulent catalytically stabilized combustion of hydrogen/air mixtures in entry channel flows. *Combust. Flame* **2005**, *140*, 70−92.

DOI: 10.1021/acs.energyfuels.7b02011
Energy Fuels 2017, 31, 11448−11459

(43) Appel, C.; Mantzaras, J.; Schaeren, R.; Bombach, R.; Kaeppeli, B.; Inauen, A. An experimental and numerical investigation of turbulent catalytically stabilized channel flow combustion of hydrogen/air mixtures over platinum. *Proc. Combust. Inst.* **2002**, *29*, 1031−1038.

(44) Kee, R. J.; Rupley, F. M.; Miller, J. A. *Chemkin II: A Fortran chemical kinetics package for the analysis of gas-phase chemical kinetics*; Report No. SAND89-8009B; Sandia National Laboratories: Albuquerque, 1996.

(45) Coltrin, M. E.; Kee, R. J.; Rupley, F. M. *Surface Chemkin: A Fortran package for analyzing heterogeneous chemical kinetics at the solid surface-gas phase interface*; Report No. SAND90-8003C; Sandia National Laboratories: Albuquerque, 1996.

(46) Schultze, M.; Mantzaras, J.; Bombach, R.; Boulouchos, K. An experimental and numerical investigation of the hetero-/homogeneous combustion of fuel-rich hydrogen/air mixtures over platinum. *Proc. Combust. Inst.* **2013**, *34*, 2269−2277.

(47) Sui, R.; Es-sebbar, E.; Mantzaras, J.; Bombach, R. Homogeneous ignition during fuel-rich $H_2/O_2/N_2$ combustion in platinum-coated channels at elevated pressures. *Combust. Flame* **2017**, *180*, 184−195.

(48) Mantzaras, J.; Appel, C. Effects of finite rate heterogeneous kinetics on homogeneous ignition in catalytically stabilized channel-flow combustion. *Combust. Flame* **2002**, *130*, 336−351.

(49) Lutz, A. E.; Kee, R. J.; Miller, J. A. *SENKIN: A Fortran program for predicting homogeneous gas phase chemical kinetics with sensitivity analysis*; Report No. SAND87-8248; Sandia National Laboratories: Albuquerque, 1996.

(50) Glassman, I. *Combustion*, 3rd ed.; Academic Press: London, UK, 1996.

(51) Mantzaras, J.; Benz, P. An asymptotic and numerical investigation of homogeneous ignition in catalytically stabilized channel flow combustion. *Combust. Flame* **1999**, *119*, 455−472.

(52) Klauck, M.; Reinecke, E. A.; Kelm, S.; Meynet, N.; Bentaib, A.; Allelein, H. J. Passive auto-catalytic recombiners operation in the presence of hydrogen and carbon monoxide: Experimental study and model development. *Nucl. Eng. Des.* **2014**, *266*, 137−147.

(53) Kyritsis, D. C.; Coriton, B.; Faure, F.; Roychoudhury, S.; Gomez, A. Optimization of a catalytic combustor using electrosprayed liquid hydrocarbons for mesoscale power generation. *Combust. Flame* **2004**, *139*, 77−89.

(54) Schneider, B.; Karagiannidis, S.; Bruderer, M.; Dyntar, D.; Zwyssig, C.; Guangchun, Q.; Diener, M.; Boulouchos, K.; Abhari, R. S.; Guzzella, L.; Kolar, J. W. Ultra-high-energy-density converter for portable power. In *Power-MEMS 2005*, Tokyo, Japan, Nov 28−30, 2005.

DOI: 10.1021/acs.energyfuels.7b02011
Energy Fuels 2017, 31, 11448−11459